ECS Journal of Solid State
Science and Technology

Metallic Nitride and Carbide Perovskites: History and Prospects

ECS Journal of Solid State Science and Technology, 2022 **11** 055002

Metallic Nitride and Carbide Perovskites: History and Prospects

J. M. D. Coey,[1,z] D. Givord,[2,a] and D. Fruchart[2]

[1]*School of Physics, Trinity College, Dublin 2, Ireland*
[2]*Institut Néel CNRS, F-38042, Grenoble Cedex 9, France*

Energy-level diagrams for cubic metallic Fe_4N and Mn_4N were proposed by Goodenough in the late 1960s. Fe_4N is ferromagnetic, but Mn_4N is ferrimagnetic with a large moment on Mn^c at the cube corner site and a much smaller antiparallel contribution from Mn^f at the three face-centre sites. Neutron diffraction revealed noncollinear ferrimagnetism with no compensation where the Mn^f moments form 120° triangular antiferromagnetic sublattices but are tilted out of the kagome (111) planes to give the small net sublattice moment. A rich variety of magnetic ordering exists in the ternary $Mn_{3-x}M'_xN$ metallic perovskites. Partial substitution of nonmagnetic M′ on Mn^c sites leads to a tunable ferrimagnetic compensation point. Two possible antiferromagnetic modes in the kagome planes are a topological Γ^{4g} mode, and a nontopological Γ^{5g} mode where the in-plane components of the Mn^f spins lie, respectively, perpendicular and parallel to the edges if the triangles in the kagome planes . Interest in the metallic perovskites has revived with the availability of high-quality thin films that facilitate measurements of magneto-transport properties, strain effects and spin wave velocity. The range of magnetic structures, magnetotransport, magnetocaloric and magnetovolume effects is exceptionally large. The topological ferrimagnets exhibit large anomalous Hall effects. The magnetism is compared with materials where N is replaced by C.

 [DOI: 10.1149/2162-8777/ac6695]

Manuscript submitted January 31, 2022; revised manuscript received March 21, 2022. Published May 2, 2022. *This paper is part of the JSS Focus Issue on Focus Issue In Honor of John Goodenough: A Centenarian Milestone.*

The metallic perovskites are an extensive family of interstitially modified cubic magnetic alloys, with ideal composition $M^f{}_3M'^cX$; their structural and magnetic properties were summarized in a volume of Landolt Börnstein, published in 1988.[1] Here M is a 3*d* element that occupies the face centre (f) sites in an fcc lattice, M′ is an element of similar atomic or metallic radius from the 4th, 5th or 6th periods that occupies the cube corner (c) site and X is a small atom, usually nitrogen or carbon that occupies the body-centre interstitial site. These materials, their parent M_4X compounds and alloys where the M atoms on c-sites are partially substituted by M′ atoms exhibit interesting and varied magnetic properties. The fully-substituted compositions $M^f{}_3M'^cX$ are also known as antiperovskites because their crystal structure, if not their crystal chemistry, is analogous to that of the insulating oxide perovskite $CaTiO_3$. The interstitial metallic compounds were intensely studied in bulk form during the period 1960–1980 and they have recently become a topic of intense interest after it was possible to grow high-quality thin films which exhibit features such as extreme strain sensitivity, perpendicular anisotropy and topological magnetism when M=Mn that are of interest for spintronics and other applications. The magnetism of metallic manganese is especially rich—and frustrating. Different polymorphs of the element are simple antiferromagnets, a complex noncollinear antiferromagnet or a spin liquid. A rough rule of thumb is that manganese atoms on sites with the shortest Mn–Mn bonds < 240 pm are nonmagnetic, those with bonds in the range 250–280 pm have small itinerant moments that couple antiferromagnetically, and those with bonds > 290 pm have large moments that couple ferromagnetically,[2] Here we outline the 60-year history of the metallic perovskites, both to help orient newcomers to the field and to highlight the contribution of John Goodenough from a period of his career when his main interests were in Magnetism and the Chemical Bond. It was a time when the authors were embarking on their research careers in Grenoble.

Results

The M_4N compounds, M=Mn, Fe, Co, Ni.—We begin with the binary interstitial compounds of the magnetic 3*d* metals. Although the face-centred cubic (fcc) structure (Fig. 1a) is the most stable only for Ni, the other three have fcc polymorphs, which may be stabilized by a small 2*p* interstitial atom in the body centre site (Fig. 1b). Corner- and face-centre sites in the fcc lattice form four equivalent cubic sublattices, but 3:1 atomic order is possible in the $L1_2$ structure (Fig. 1c). Occupancy of the octahedrally-coordinated 1*b* body-centre site by a 2*p* element renders the 1*a* corner site (c) and the 3*c* face-centre sites (f) in the P*m*-3*m* space group crystallographically inequivalent; they may be occupied by the same atoms M as in Fig. 1b or different atoms M′ and M in the perovskite structure (Fig. 1d). The 3*d* atoms have a metallic radius r_m of about 125 pm and the radii of 4*d* and 5*d* atoms are a little bigger ≈ 135 pm. The radius of the octahedral interstice in the close-packed 3*d* structure is much smaller, $(\sqrt{2}–1)r_m = 52$ pm, so only the smallest atoms can squeeze in, which limits the choice to the least electronegative 2*p* elements, boron, carbon and nitrogen. All are bigger than the space available, so interstitial occupancy produces significant lattice dilation. Rarely is M_4X absolutely stable at low temperature.[3] In the case of iron, Fe_3C is much more stable than Fe_4C, but Fe_4N does appear on phase diagrams. Likewise for manganese, Mn_4C is a high-temperature phase ($Mn_{23}C_6$ is the stable compound) but Mn_4N appears on the phase diagram. First, we discuss Fe_4N, and then the other binary nitrides.

The atomic radius of iron suggests a lattice parameter a_0 for fcc iron of $2\sqrt{2}r_m = 354$ pm, where calculations show no spontaneous spin polarization of the 3*d* band, but if a_0 is increased to 380 pm, the value for Fe_4N, the iron becomes a strong ferromagnet with a fully-occupied majority-spin sub-band.[2] The Curie temperature $T_C = 769$ K; there is a large moment of 2.96 μ_B on Fe^c at the 1*a* corner site and a smaller moment of 2.1 μ_B on Fe^f at the 3*c* face center sites where iron is covalently bonded to nitrogen. The different moments on the two sites were established by the early neutron diffraction study of Fraser.[4] The 1*a* Fe^c moment is augmented by charge transfer to 3*c* Fe^f and N, The average iron moment of 2.22 μ_B is the same as for bcc iron, but the atomic volumes in the bcc and expanded fcc structures are 0.0118 nm^3 and 0.0137 nm^3 per iron atom, respectively, giving a room-temperature magnetization *M* of 1.71 MAm^{-1} for αFe and 1.51 $MAm^{-1}$for Fe_4N. It is magnetization—the magnetic moment per unit volume—rather than the atomic moment *m* that counts in most ferromagnetic applications. Three consequences of the interstitial occupancy are therefore lattice dilation, covalent bonding and charge transfer.

Next we consider Mn_4N. Here the magnetic moment per formula unit at room-temperature is only 0.77 μ_B at room temperature, an

[a]Deceased.
[z]E-mail: jcoey@tcd.ie

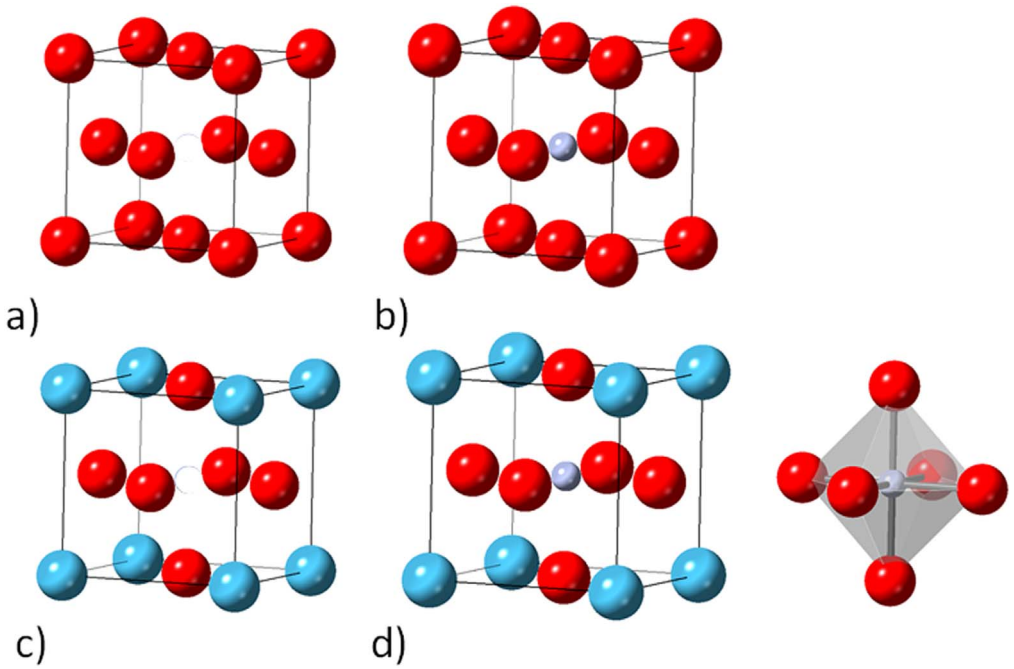

Figure 1. Crystal Structures (a) face-centred cubic, (b) $L1_2$ (c) M_4N, M = Mn—Ni, (c) $M_3M'X$ perovskite (Space group P*m*-3*m*), showing the XM_6 octahedron. M atoms are red, M′ atoms are blue and the X atom is gray. In the text, atoms with superscript c are on 1*a* corner sites, atoms with a superscript f are on 3c face-centre sites and X = N or C atoms occupy the 1*b* body-centre site.

order of magnitude less than for Fe_4N, although the magnetic ordering temperature, $T_C = 755$ K, is similar. The net magnetization lies along a [111] easy direction, as it does in Fe_4N. The small net moment indicates ferrimagnetic order, but the variation of magnetization as a function of temperature shown in Fig. 2 is quite unusual, with a steep initial decline at low temperature but there is no compensation point below the ferrimagnetic Néel temperature T_c. Early neutron diffraction studies at 77 K found antiparallel moments of 3.85 μ_B and −0.9 μ_B on 1*a* and 3*c* sites, respectively[5] yet no combination of inter—and intra-sublattice exchange interactions is able to reproduce a curve of this shape for two-sublattice collinear ferrimagnetism, using molecular field theory constrained by $M(0)$ and T_c.[6]

The key to resolving this problem was found in a 1979 powder neutron diffraction study with polarization analysis carried out in Grenoble at the ILL.[7] That study was followed by many other investigations of compounds and solid solutions,[1] where Mn^c is replaced, for example, by a nonmagnetic atom such as Ga, or N is replaced by C.[8] The projection of the 3*c* sublattice moments along the [111] ferrimagnetic axis is a fraction of their larger, noncollinear moments. The (111) planes of 3*c* sites form a kagome lattice shown in Fig. 3b), where the Mn^f–Mn^f separation of 273 pm is in the range for delocalized manganese *d*-electrons and antiferromagnetic exchange.[2] The 3c sublattice is therefore frustrated. The in-plane components of a triangle of three atoms in the (111) plane have no net magnetization. They follow one of two symmetry-allowed spin configurations, Γ^{4g} and Γ^{5g}, with three sublattice moments at 120° to each other in a triangular antiferromagnetic structure. The spins lie either perpendicular or parallel to the sides of the triangle, as illustrated in Figs. 3b–3e). When coupled antiparallel to the ferromagnetic 1*a* sublattice whose moment lies in the [111] direction (the Mn^f–Mn^c separation is also 273 pm), the 3c moments tilt by an angle θ out of the (111) plane towards the [−1–1–1] direction producing the "umbrella" ferrimagnetism of the Γ^{4g} mode, illustrated in Fig. 3f) Recent constrained density functional theory calculations find the magnitude of the total 3*c* moment at room temperature is close to 2.4 μ_B and the tilt angle θ is near to 20°.[6]

Bulk, stoichiometric Co_4N has not been prepared, but ferromagnetic thin films have been grown that are stable up to 525 K, where

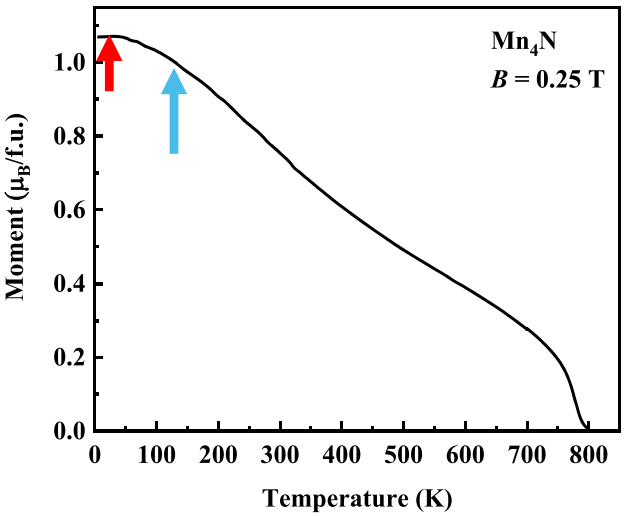

Figure 2. Temperature-dependence of the magnetization of Mn_4N.[6]

they lose their nitrogen. The average Co moment is enhanced to 1.85 μ_B, but the magnetization $M_s = 1.35$ MAm^{-1} is similar to that of pure cobalt. The Curie temperature cannot be measured, but calculations gave 827 K.[10] Pure fcc Co has a Curie temperature of 1388 K.

The Ni_4N compound can have a slightly different, tetragonal structure with two cubic unit cells stacked vertically to give a tetragonal cell with c/a = 1.96. The nitrogen position shifts from ½ ½ ½, the body centre of the original cubic cell to 0, 0, ½ in the upper cubic cell.[11] Thin films are paramagnetic[12] but extrapolation of data on $(Fe_{1-x}Ni_x)_4N$ powders to x = 1 suggests a moment of 0.2 μ_B/Ni at low temperature and $T_c = 125$ K.[13] Properties of M_4N compounds are summarized i Table I.

The metallic perovskites $M_3^fM^cX$.—Although the cubic structures of metallic $M_3M'X$ compounds formally resemble that of the mineral perovskite, $CaTiO_3$, the analogy is tenuous. Oxide perovskites ABO_3

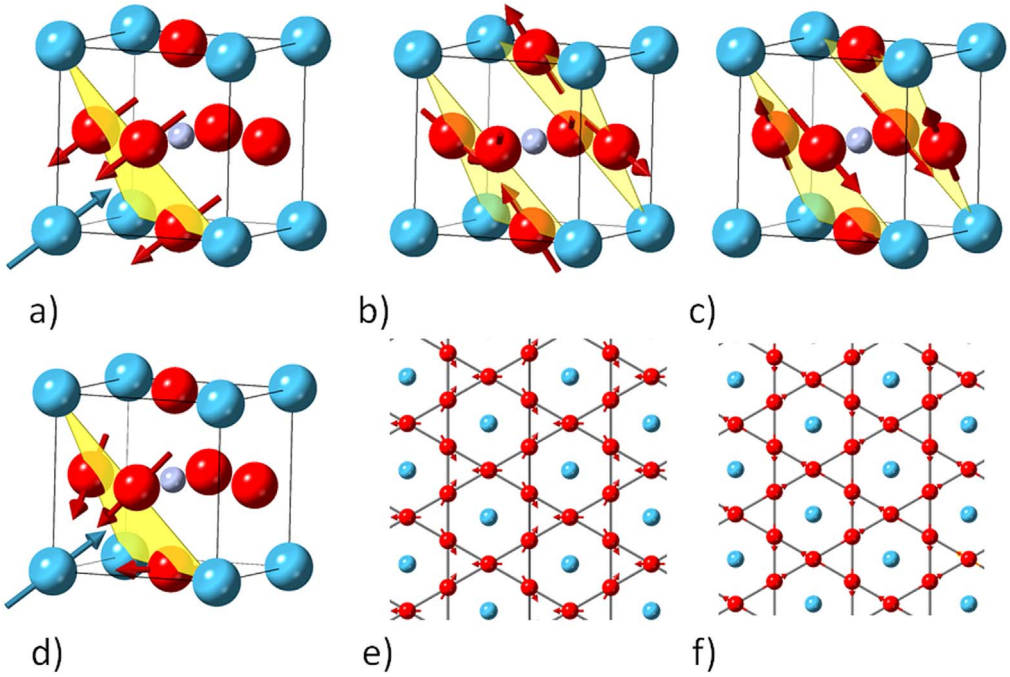

Figure 3. Magnetic structures (a) Collinear ferrimagnetism, (b) and (c) 120° triangular antiferromagnetic modes Γ^{4g} (b) and Γ^{5g} (c) for $Mn^{f,}$ which forms (111) kagome sheets with the corresponding spin orientations shown below for Γ^{4g} (e) and Γ^{5g} (f) M'^{c} here is nonmagnetic. (d) The Γ^{4g} noncollinear ferrimagnetic mode.

Table I. Properties of the M_4N interstitial compounds.

Compound	Structure	Space group	a_0 a, c pm	T_c K	Moment/fu μ_B (RT)	Magnetic order
Mn_4N	cubic	P*m*-3*m*	386	755	1.1 1*a* 3.8; $3c^{\|\|}$ 0.9; $3c^{tot}$ 2.0	triangular ferrimagnet
Fe_4N	cubic	P*m*-3*m*	380	769	9.0 1*a* 3.0; 3*c* 2.0	ferromagnet
Co_4N	cubic	P*m*-3*m*	370	n.d.	7.4[a)]	ferromagnet
Ni_4N	tetragonal	P4*mm*	372, 728	(125)	—	paramagnet

a) thin film.[9]

are insulating ionic compounds with O^{2-} anions at the face centre sites and highly-charged cations on the corner and body-centre sites. The numerous tetragonal, rhombohedral, and orthorhombic variants of the basic cubic structure are related to twists and tilts of the corner-sharing BO_6 octahedra, governed by a ratio of ionic radii given by the tolerance factor $t = (r_A + r_O)/\sqrt{2}(r_B + r_O)$. The factor is equal to 1 for the ideal cubic structure. $CaTiO_3$ is actually orthorhombic, while $BaTiO_3$ and $SrTiO_3$ with larger A-site cations are cubic.

The metallic perovskites $M_3M'X$ (sometimes called "antiperovskites" or "inverse perovskites") are quite different. Bonding is metallic, at least for M and M′, which form a stable cubic close-packed $L1_2$ Cu_3Au-type structure where the body-centre X (or A) site is so small that few 2*p* elements are able to enter and bind covalently with their six metallic neighbours in a stable XM_6 octahedron. The formal charge of the nitrogen was found to lie between −0.6 and −1[14] but interstitial carbon is neutral and the carbides are less stable.

Goodenough discussed metallic bonding in a 1960 paper in Physical Review.[15] The 3*d* metals have both localized and delocalized electron orbitals. In the fcc structure, delocalized electrons occupy the t_{2g} orbitals d_{xy}, d_{yz}, d_{zx} that are each directed towards four neighbouring face-centre sites lying in the *ij* plane, whereas the partially localized electrons occupy the e_g orbitals d_{z^2} and $d_{x^2-y^2}$ that are directed between the nearest-neighbor atoms The bonding can stabilize the fcc structure for the t_{2g}^6 atoms Fe, Co and Ni. A body-centre interstitial atom was introduced in later schematic energy level diagrams such as those reproduced in Fig. 4 for Fe_4N and Mn_4N assuming a N^- charge state. Goodenough developed his ideas in a comprehensive 85-page MIT report entitled "Conceptual Phase Diagrams and their Application to Itinerant Electron Magnetism"[16 b] half of which is devoted.to the metallic perovskites.

The stabilization of the $M^f{}_6N$ octahedron when nitrogen is introduced at the body-centre position in Fe_4N or Mn_4N facilitates partial or complete substitution of a different metallic element from the fourth fifth or sixth periods in the M^c site, producing rich range of ordered magnetic metals, solid solutions and magnetic structures, many of which were studied by neutron diffraction and other methods in the 1970s[1,17–19] Existence maps of the interstitial phases are provided in the Landolt Börnstein volume[1] for all the 3*d* transition metals. Two of the diagrams, for M^f = Mn and Fe, are shown in Fig. 5.

The existence maps refer to compounds where the M = Mn or Fe at the corner site is completely replaced by another M′ element. Materials investigated by neutron diffraction included some solid solutions between nitrides and carbides, or between different M′ atoms. The two phase diagrams in Fig. 6 give an idea of the complexity, especially when M^f = Mn. Fig. 6a) shows the effect of

[b]Available on request from DF daniel.fruchart@orange.fr or JMDC jcoey@tcd.ie.

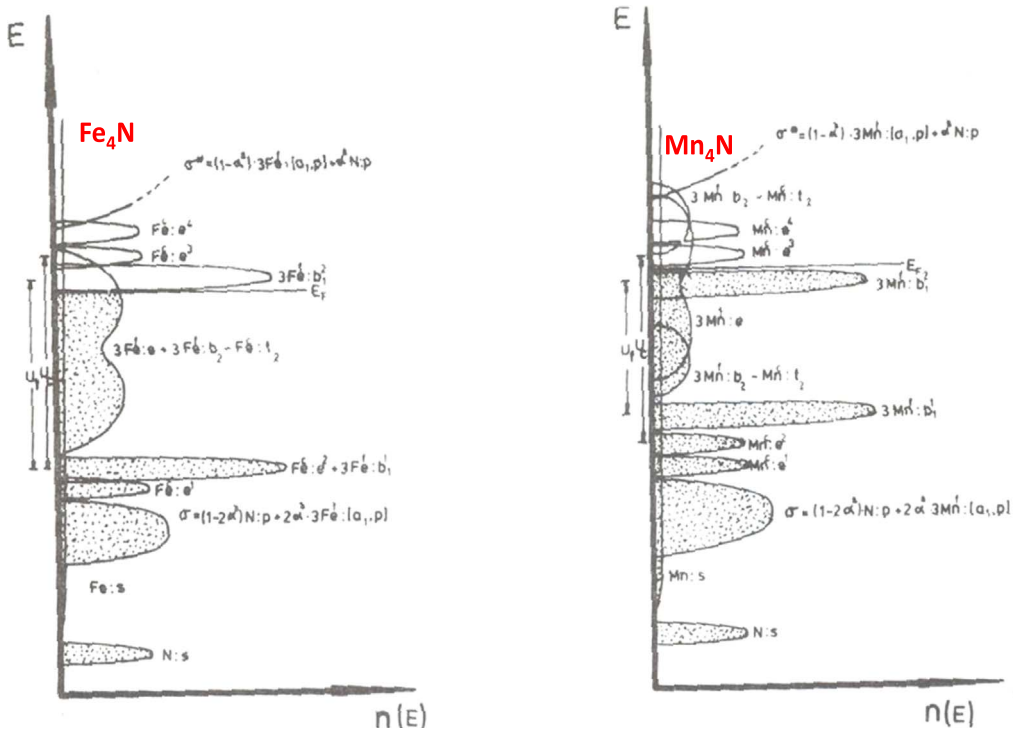

Figure 4. Goodenough's schematic energy-level diagrams for Fe_4N and Mn_4N.[16]

Mg							Al		
	Mn	Fe	Co	Ni	Cu	Zn	Ga	Ge	As
			Rh	Pd	Ag		In	Sn	Sb
Mn			Ir	Pt	Au	Hg	Tl	Pb	

Mg							Al		
	Mn	Fe	Co	Ni	Cu	Zn	Ga	Ge	As
			Rh	Pd	Ag		In	Sn	Sb
Fe			Ir	Pt	Au	Hg	Tl	Pb	

Figure 5. Existence maps of $M^f{}_3M'^cN$ (yellow) and $M^f{}_3M'^cC$ (grey). Dark yellow shows that either N or C is possible. The metal M = Mn or Fe is indicated in red in the bottom left corner, and various possible M′ atoms are in black. [after Ref. 1].

progressive substitution of a nonmagnetic element, gallium, for Mn^c in $Mn_{4-x}Ga_xN$. In the end-member, x = 0, the noncollinear ferrimagnetic structure evolves with temperature as the triangular mode changes from Γ^{4g} to Γ^{5g}. The second-order ferrimagnetic Néel temperature decreases monotonically up to x = 0.8, and the system exhibits a compensation temperature in the range of substitution $0.18 < x < 0.30$, with $x_{comp} = 0.26$ at room temperature. The slope of the decrease of T_c and the slope of T_{comp} or the width of the compensation region depend both on the valence of M′, the tilt angle θ of the Mn^f sublattice and the change of lattice parameter, which is negligible in the case of Ga. Gallium is good, because it allows T_{comp} to be tuned with no strain and little change of T_c. Then at $x \approx 0.9$, ferrimagnetic order gives way to pure Γ^{5g} triangular antiferromagnetism, and the transition at the Néel point becomes first order.

The effect of substituting C for N in $Mn_3GaN_{1-y}C_y$ is illustrated in Fig. 6b). When $y > 0.07$, the triangular antiferromagnetism gives way to Mn_3CuN-type noncollinear ferromagnetic order with a tetragonal ($\sqrt{2}$a, $\sqrt{2}$a, a) unit cell and a [001] easy axis. The transition remains 1st order. Then at y = 0.5, Mn_3GaC-type antiferromagnetism takes over; two ferromagnetic (111) sheets in the simple unit cell are coupled antiferromagnetically, and the transition at the Néel point becomes second order, with notable short-range order above T_N. Finally, when $y > 0.85$ the antiferromagnetism gives way to a ferromagnetic phase at a first-order antiferromagnetic to

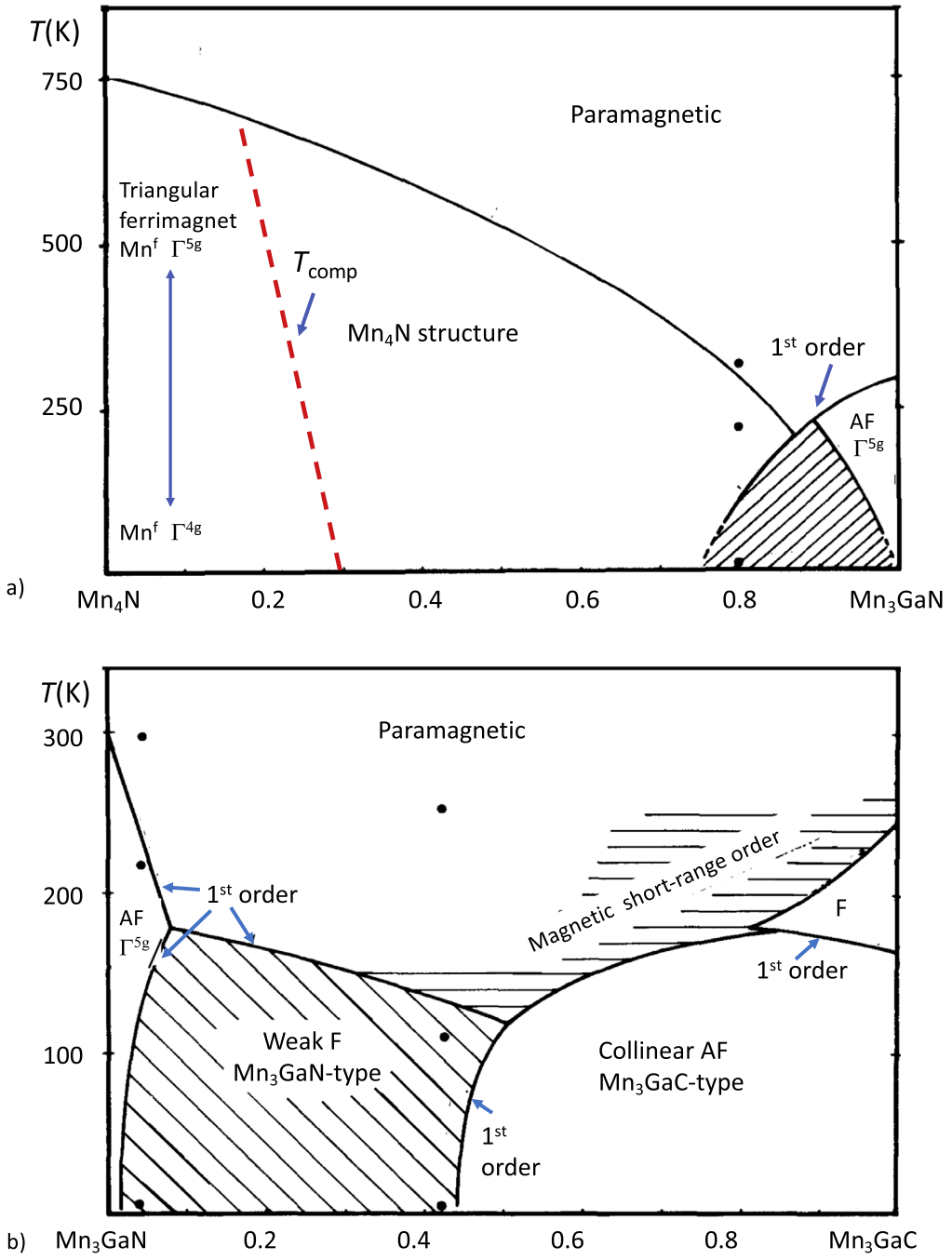

Figure 6. Magnetic phase diagrams of the solid solutions top $Mn_{4-x}Ga_xN$ and bottom $Mn_3GaN_{1-y}C_y$. [after Refs. 8 and 6]. The behavior is described in the text.

ferromagnetic (AF → F) phase transition at 170 K. The Curie temperature is 240 K.

A magnetic phase diagram of the solid solutions of $Mn_3{}^f$ M′N between five adjacent M′ elements in the Ni—Ge series is shown in Fig. 7.[20,21] The different magnetic phases encountered on this diagram are summarized in Table II and Fig. 8.

After an initial report in 1966,[20] the AF → F transition in Mn_3GaC in Fig. 6b was investigated in magnetic fields up to 23 T and in hydrostatic pressures up to 500 Mpa in a 1969 thesis aimed at better understanding the magnetism of manganese in the metallic state.[23] Data were included on most of the thermodynamic aspects of the 1st order AF → F transition in the parent compound, as well as the influence of carbon vacancies and Zn substitution for Ga to modify the electronic properties. The magnetization is similar in both cases, either in an applied magnetic field (Fig. 9) or under external pressure. Furthermore, neutron diffraction showed that the complex and non-collinear magnetic structures of Mn_3ZnN $Mn_3GaC_{0.935}$ were similar. Those of Mn_3CuN and Mn_3SnC were identical.[1]

These experiments may be regarded as precursors of the studies of magnetocaloric and barocaloric effects that came into vogue about 30 years later. At the time, those labels were not in use by the community dealing with fundamental and applied studies of magnetic refrigeration, which was not the motivation of the work. The 1st order AF → F transition in Mn_3GaC is classified as an inverse caloric effect, like the one in FeRh, and not the more common 2nd order F → Para direct magnetocaloric effect. Three immediate impacts of this early study, which was followed by many other results on Mn_3GaC and related magnetocaloric materials,[24–27] can be identified.

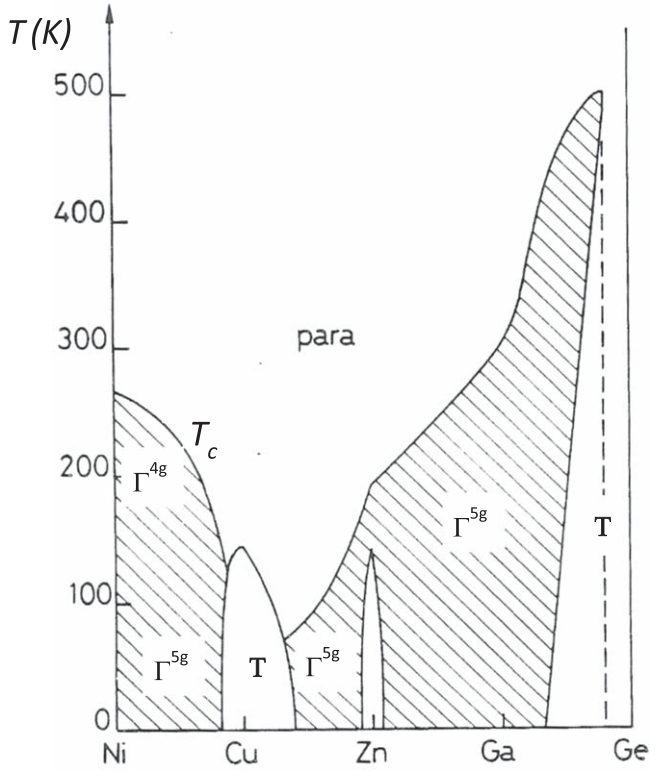

Figure 7. Magnetic phases for $Mn_3M'N$ for M' from the 4th period.[22] The triangular AF mode Γ^{5g} is mostly stable, except for low temperature ranges around Cu and Zn and at the Ge limit, where tetragonal distortions occur. The Γ^{4g} AF mode is stabilized for Mn_3NiN in the highest temperature range, with a weak F [111] component. For M' belonging 5th period, a similar scheme is found.

1. The fundamental thermodynamics of the 1st order AF → F transition and its behavior under high magnetic field and isostatic pressure was clarified for Mn_3GaC by varying the carbon or zinc doping of the material. The data as a function of temperature in constant applied magnetic field on the one hand or under constant pressure on the other hand, lead to consideration of the entropy variations in terms of the Clapeyron Eqs. 1 and 2:

$$S_F - S_{AF} = V_F - V_{AF}/(\partial T_T/\partial p)_H \quad [1]$$

$$S_F - S_{AF} = M_F - M_{AF}/(\partial T_T/\partial H)_p. \quad [2]$$

The equations give very similar values for the total entropy change, ΔS_T: 1.18 ± 0.1 kJ kg^{-1}.K and 1.14 ± 0.2 kJ $kg^{-1}.K^{-1}$, respectively. However, the variation of lattice entropy calculated from the volume change at the transition ($(V_F–V_{AF})/V \sim -0.45\%$) is $\Delta S_L \sim -0.36$ kJ$kg^{-1}.K^{-1}$. The disagreement with Eqs. 1 and 2 demonstrates that a simple change of sign of the exchange cannot be the explanation. Moreover, based on a molecular field model, it was anticipated from the magnetization data that $S_m = NM_0'^2/T.(1—M'/M_0')$ with M' and M_0', being the magnetization at the transition and the saturation magnetization, respectively. The coefficient $NM_0'^2/T$ markedly favors the AF reference state so (S_F—S_{AF}) must be negative. From magnetic entropy considerations alone, Mn_3GaC should be antiferromagnetic up to highest temperature. Hence the change of entropy associated with the electronic configuration at the transition must be the predominant term. The magnetic configuration of Mn changes markedly as the Mn moment falls from 1.8 μ_B (AF) to 1.2 μ_B (F). The change of entropy was later shown to be very large, 15 kJ$kg^{-1}K^{-1}$ in 2 T.[26] Direct measurements of the temperature change upon adiabatic application of magnetic field gave $\Delta T \sim -5$K over a wide temperature range below the transition, practically independent of the initial temperature and field,[24]

2. The results stimulated further investigations the antiferromagnetic and ferromagnetic structures, both of Mn3GaC,[8] and also of representative members of the $Mn_3M'X$ series (M′ = Zn, Ga, Sn with X = C; M′ = Ni—Ga, Rh—Sb, and Pt with X = N),[28] especially by means of neutron diffraction. The investigations were extended to a systematic analyses of complete sets of magnetic and crystallographic phase diagrams, such as those summarized in Fig. 7. The Mn3GaN type of triangular antiferromagnetism and its variants were discovered and analysed[19,28,29] using the magnetic irreducible representation concept developed by Bertaut.[30] Many compounds or solid solutions in the Mn3MX series were shown to exhibit either the Γ^{5g} (AF) or Γ^{4g} (AF) +F triangular configurations, depending on composition and temperature (Fig. 3).
3. The work chimed with John Goodenough's interest in quantifying the electronic and magnetic parameters involved in different bonding schemes for manganese in its various alloys and compounds. It stimulated him to clarify the configuration scheme driving the relative distribution of 3*d* to 4*s* electrons , as well as the distribution in different bonds (distance and electron density). Goodenough wrote his comprehensive report[16] shortly afterwards.

Thin films

Recent years have witnessed a sharp revival of interest in Mn_4N-based materials, in thin film form, motivated in part by the emergence of the new field of ferrimagnetic spin electronics[31] Two recent reviews, one by Suemasu et al.[32] on the status of Mn_4N based ferrimagnets, the other by Zhang and Mi[33] on Mn_4N-based ferrimagnetic thin films for spintronics include extensive bibliographies. Our

Table II. Magnetic structures of some metallic Manganese metal perovskites Mn_3 M′X, where M′ is nonmagnetic and X = N, C.[1] Crystal structure type refers to Fig. 8.

Type	Magnetic unit cell	Magnetic structure	Examples
f	cubic a_0	Ferromagnet [111]	Mn_3AlC, Mn_3GaC (>165 K)
a	cubic a_0	Triangular AF Γ^{5g}	Mn_3AgN, Mn_3ZnN, Mn_3GaN, Mn_3SnN
b	cubic a_0	Triangular AF Γ^{4g}	Mn_3NiN, Mn_3AgN, Mn_3SnN
c	tetragonal $\sqrt{2}a,\sqrt{2}a,2a$	Non Collinear AF	Mn_3ZnN (< 140 K)
e	cubic a_0	Collinear AF	Mn_3GaC (< 165 K)
g	tetragonal $\sqrt{2}a,\sqrt{2}a,2a$	Ferrimagnet	Mn_3ZnC (< 231 K)
d	tetragonal $\sqrt{2}a,\sqrt{2}a,a$	Ferrimagnet	Mn_3SnC, Mn_3CuN
h	cubic a_0	Ferromagnet [001]	Mn_3ZnC (> 231 K)
	tetragonal $a,a,2a$	Non Collinear AF	Mn_3RhN_x, Mn_3PtN_x
	tetragonal $a,a,2a$	Non Collinear AF	Mn_3SnN (> 357 K)
	tetragonal a,a,na	Incommensurate AF	Mn_3SnN (< 237 K)
	tetragonal $a,a,2a$	Non Collinear AF	Mn_3SbN

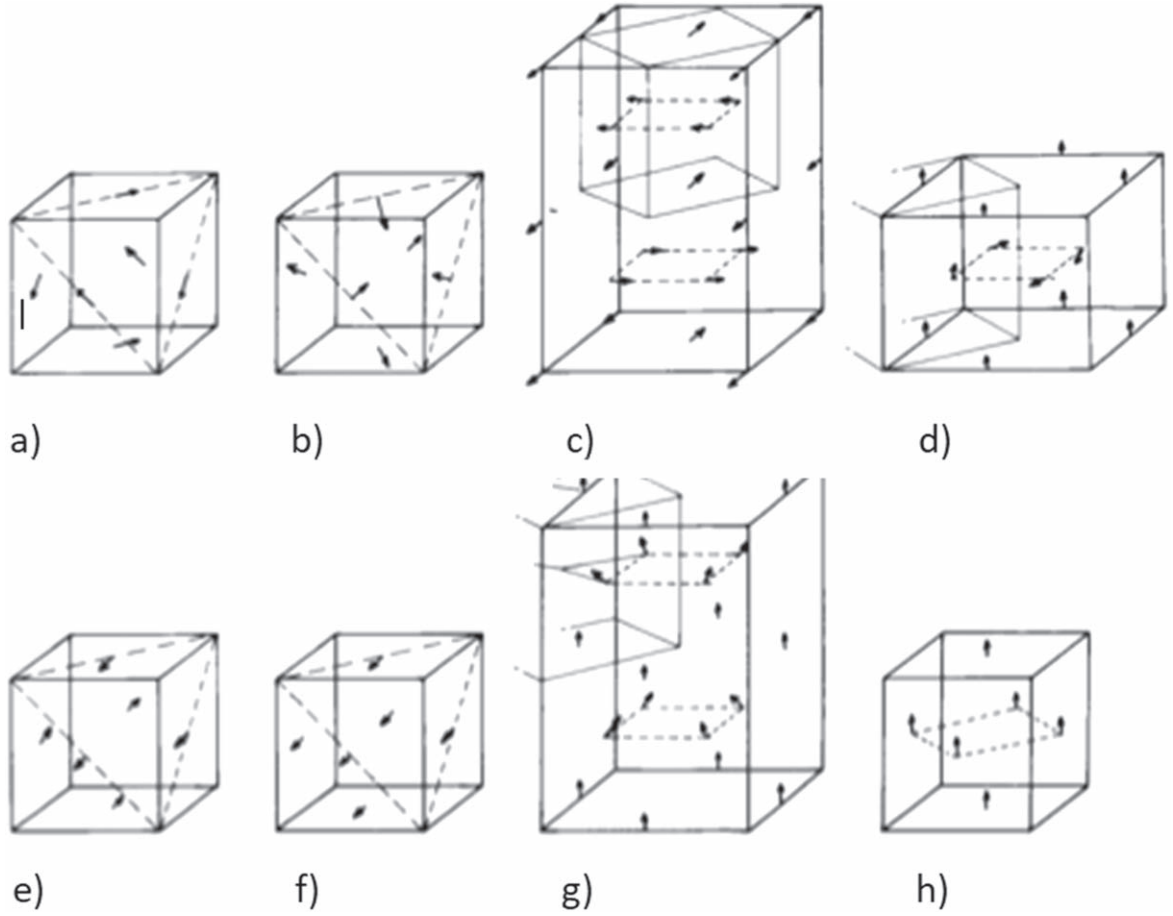

Figure 8. Magnetic structures of some ternary $Mn_3{}^{f}$ M′X phases.[21] (a) (111) AF Γ^{5g} mode e.g. Mn_3GaN, (b) AF-(111) Γ^{4g} mode, compatible with F-[111] (Mn_3NiN, Mn_3AgN, Mn_3MnN, Mn_4N), (c) Low temperature AF arrangement for Mn_3ZnN in a a$\sqrt{}$ a$\sqrt{2}$ × a$\sqrt{2}$ × c magnetic supercell, the high temperature AF mode is Γ^{5g}, (d) Ferrimagnetic structure Mn_3CuN in a a$\sqrt{2}$ × a$\sqrt{2}$ × c supercell. The structure is the same for Mn_3SnC with one less *sp* X valence electron, but three more M′ *sp*-valence electrons, (e) [111] AF structure of Mn_3GaC below 164 K, the (111) F planes are oppositely aligned along [111], (f) F[111] structure for Mn_3GaC from 165 K to T_C, (g) Non-collinear ferrimagnetic structure for Mn_3ZnC below 231 K in a$\sqrt{2}$ × a$\sqrt{2}$ × c supercell. With one more M′*sp* valence electron and one less X *sp* valence electron (X = $C_{0.935}$), the magnetic arrangement is quite similar for $Mn_3GaC_{0.935}$, (h) High temperature ferromagnetic structure of Mn_3ZnC, similar to that of Mn_3GaC (f) except the easy direction is now [001], The more complex ferrimagnetic structures of Mn_3SbN and Mn_3SnN are not illustrated.

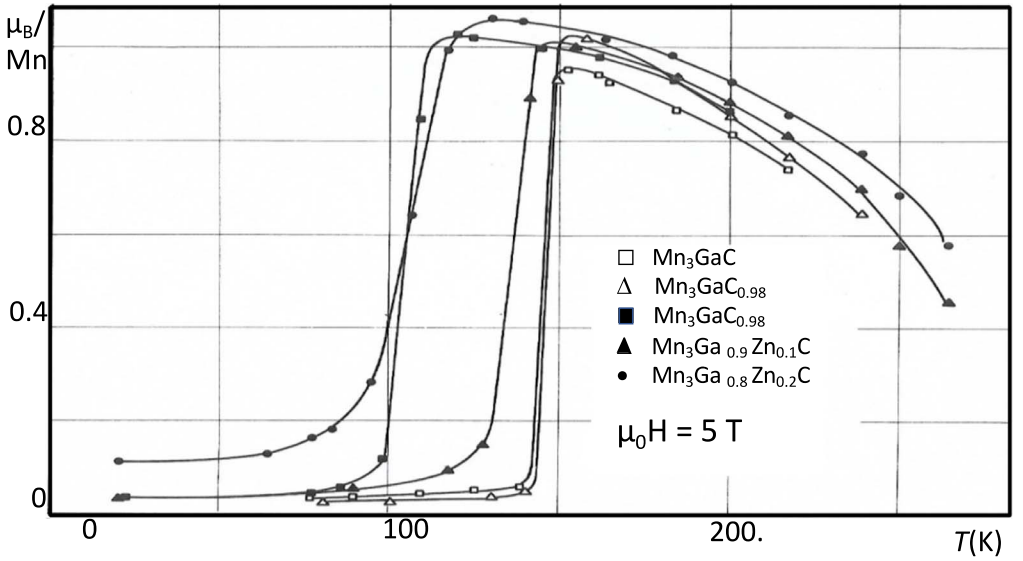

Figure 9. Thermomagnetic curves of Mn_3GaC in 5 T showing the 1st order AF → F transition. C vacancies and Zn substitution both shift the transition to lower temperature.[23]

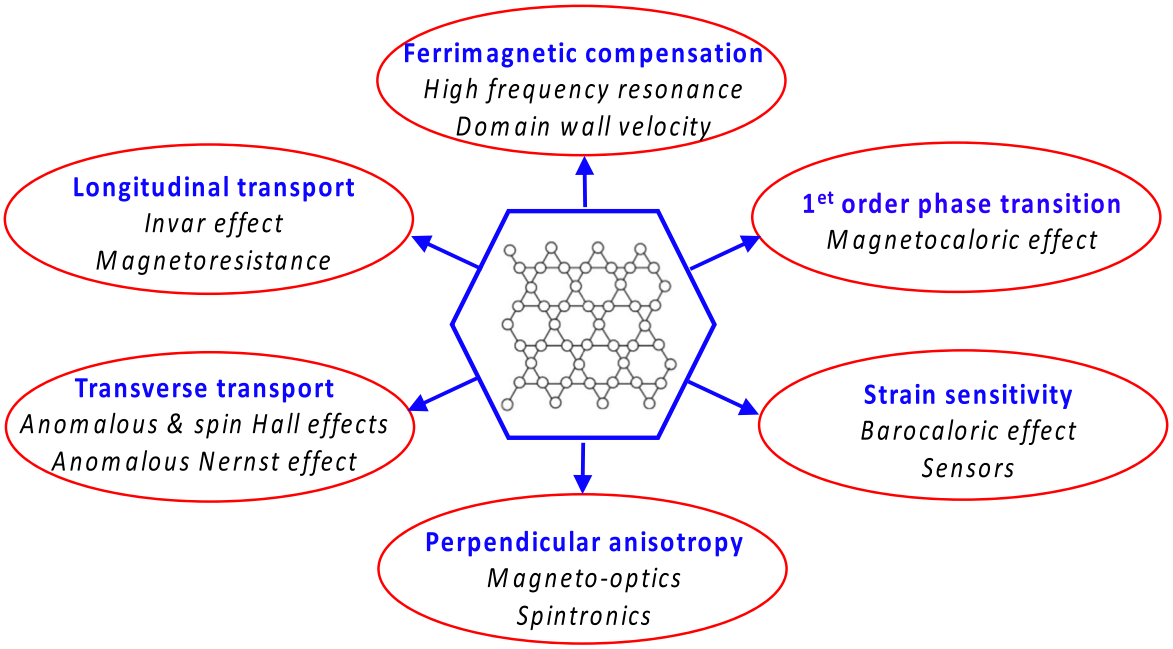

Figure 10. Overview of the physical properties of metallic manganese-based perovskites, due to frustrated antiferromagnetic interactions in the Mn^f kagome sheets.

aim here is not a comprehensive review, rather a short overview to highlight reasons for the interest in these materials, set in the context of established knowledge of the bulk materials which has been rather overlooked.

The materials exhibit an unusual range of potentially useful features[c], some of them related to the ability to tune compensation by strain or temperature, some related to fast spin dynamics and others stemming from the magnetic topology. Most, if not all of these of the interesting features derive from frustrated antiferromagnetic interactions of Mn^f in the (111) kagome sheets. The three-dimensional cubic structures involve four interconnected layers of kagome sheets, and high magnetic ordering temperatures. Figure 10 gives an overview of the various effects.

Thin films have been grown by different methods,[33] notably by molecular beam epitaxy or reactive sputtering. There are also some reports of film growth by pulsed laser deposition. The challenge is always to find the best combination of substrate, deposition temperature and nitrogen pressure, which depends on the deposition method and the deposition tool. When optimum conditions are found and published, others can follow them and scientific progress picks up speed.

Perpendicular magnetic anisotropy is necessary for the effective operation of many thin film spintronic devices and for measurements of relevant magnetic properties. The anisotropy field should exceed the magnetization of the thin film. For ferrimagnetic Mn_4N films with small net magnetization, this is achieved by substrate-induced biaxial strain. Commonly-used substrates for $Mn_{4-x}M'_xN$ are (100) $SrTiO_3$ and (100) MgO. Although the magnetic easy axis for unstrained bulk Mn_4N is [111], the tetragonal distortion induced in films with thickness of order 10 nm deposited on these substrates is of order 1%, with $c/a < 1$. The lattice parameter of the cubic substrates (391 pm for $SrTiO_3$, 421 pm MgO) is greater than that of the films ($\sim$ 386 pm) so biaxial tensile stress imposed on the film by the substrate. For MgO, where the lattice mismatch is 9%, growth cannot be epitaxial.[6] The [001] direction perpendicular to the film plane becomes the ferrimagnetic easy axis and the magnitude of the anisotropy constant is $K_1 \sim 100$ kJm^{-3}, with a saturation magnetization $M_s \sim 150$ kAm^{-1}.[34] Although $SrTiO_3$ is more convenient for magnetic measurements at low temperature because there is no Curie-law susceptibility due to traces of paramagnetic Fe^{2+} impurities in the substrate, higher deposition temperatures and squarer perpendicular hysteresis loops are achieved with MgO,[6] The noncollinear spin structures and magnetotransport properties of thin films with a [001] easy axis are expected to be different from those of bulk material with a [111] easy axis, but they have yet to be determined.

Advantages for spintronics that result from being able to use ferrimagnetic materials close to compensation[31] include insensitivity to perturbation by external magnetic fields and thermal or strain control of the anisotropy field. As a ferrimagnet approaches compensation, the anisotropy field $\mu_0 H_a = 2K_1/M_s$ diverges. The transverse magneto-transport and magneto-optic responses are often dominated by the band structure of one or other of the magnetic sublattices, so the sign changes at the compensation temperature. The spin resonances of nearly-compensated ferrimagnets are in the hundred GHz to low THz range, one or two orders of magnitude faster than for ferromagnets.

An indication of fast collective spin dynamics is the exceptionally high domain wall mobility of Mn_4N films, that allows the walls to be driven at great speed,[35] especially when the films are Ni-doped and close to compensation. There, velocities of up to 3 kms^{-1} have been reported at a current density in excess 10^{12} Am^{-2},[36] which may be related to the high magnetic resonance frequency associated with the anisotropy field that governs Walker breakdown. The walls are driven directly by adiabatic spin transfer torque, with no need to inject spin currents from an adjacent heavy metal layer. Current-induced adiabatic switching has been reported in single layers for current densities of 10^{10} Am^{-2}.[37] In these cases, the non-collinearity of the ferrimagnetism may be ignored in the framework of macrospin micromagnetism, but in atomic-scale electronic structure calculations a collinear straightjacket will inevitably give misleading results.[38]

The net ferrimagnetic magnetization of Mn_4N is exceptionally sensitive to strain, especially when the alloy is doped close to compensation, because of the sensitivity of the Mn^f–Mn^f exchange to interatomic distances in the range 280–290 pm, and the frustrated nature of the exchange-coupled kagome sheets that is responsible for the various different noncollinear magnetic structures encountered in bulk material; transitions between them are often induced by composition, temperature or strain. One manifestation of this is the

[c]Strategic concerns about the global supply of rare earth elements, which apply for bulk materials, are misplaced for thin film devices. A kilogram of rare earth could cover a million 300 mm wafers with a layer 1 nm thick.

giant piezomagnetism found in films of Mn_3NiN deposited on the poled ferroelectric $BaTiO_3$[39] offering electric field control of the magnetization. Another is the flexomagnetism when the films are bent.[40] There is a large barocaloric effect across the Néel temperature. The effects have been investigated by density functional theory in a range of metallic perovskites with frustrated noncollinear spin structures.[41–43] The effects are sensitive to atomic disorder, and the magnetic structure has a strong influence of the magnetovolume effects.[44] The converse magnetovolume effect is volume magnetostriction, and a negative coefficient of thermal expansion that leads to a compositionally tunable invar effect.[45] Giant linear magnetostriction is also reported, for Mn_3CuN.[46] The magnetovolume effects have potential applications in sensors.

We saw in the last section how a first-order AF → F phase transition of Mn_3GaC on increasing temperature, which may reflect phonon averaging of the distance-dependent exchange, is associated with an inverse magnetocaloric effect. The transition can be suppressed by carbon substoichiometry that destabilizes the antiferromagnetic state.[25] There are reports of similar effects in Mn_3CuN[47] and Mn_3ScC.[27] The barocaloric effect is related to a change of magnetic entropy under strain, which may also be used for cooling. A large effect is reported for Mn_3GaN,[48] where the entropy change at the AF→F transition near room temperature is 22.3 $Jkg^{-1}K^{-1}$ and the adiabatic change of temperature on releasing a pressure of 93 Mpa is 5 K. An even larger entropy change is found in Mn_3NiC.[49] New magnetic phases of Mn_3GaN are predicted theoretically, and a novel cooling cycle that makes use of them has been proposed[50]

Antiferromagnetic $L1_2$-structure Mn_3Ir is a favorite material for exchange bias in spintronics. The crystal structure, illustrated in Fig. 1c), has no interstitial atom. It is a triangular antiferromagnet with a very high Néel temperature (960 K in the fully-ordered state) and strong spin–orbit coupling from Ir. The compounds Mn_3M' with $M' = Rh, Ir, Pt$ are cubic, but when $M' = Ga, Ge, Sn$, they crystalize in a hexagonal structure with space group $P6_3/mmc$ with a $2a, 2a, c$ unit cell, where a, c refer to a monatomic hexagonal close-packed lattice. Both cubic and hexagonal structures are composed of kagome sheets, which are (111) sheets in the cubic variant and (0001) c-planes in the hexagonal variant.

Mn_3Ir, where the triangular antiferromagnet order is of the Γ^{4g} type illustrated in Figs. 3b and 3e was the first antiferromagnet where an anomalous Hall effect was predicted.[51] A large effect has not yet been observed experimentally in Mn_3Ir, but it has been found in Mn_3Pt, which has the same triangular antiferromagnetic structure at room temperature. The effect vanishes at 360 K, where there is a first-order phase transition with a 0.8% volume expansion to a collinear antiferromagnetic state, Switching between the two states is achieved electrically by depositing the Mn_3Pt film on a ferroelectric $BaTiO_3$ substrate.[52] Anomalous Hall effects were also predicted in the hexagonal compounds[53] and large effects have been reported in Mn_3Sn[54] and Mn_3Ge.[55] The effects arise from the topology of the coplanar triangular spin configuration of the Mn triangles.[56] Large spin Hall effects are also expected to also result from the noncollinear triangular antiferromagnetic spin structures in Mn_3 M' compounds,[57] even in the absence of spin–orbit coupling[58] They are reduced by spin–orbit interaction or a tilting of the spins out of the plane.[59] A very large spin Hall effect of 35% has been observed in Mn_3Ir.[60]

The triangular $Mn_{4-x}M'_xN$ ferrimagnetis perovskites also exhibit large anomalous Hall effects. Anomalous Hall conductivity has been calculated for many $Mn_3M'N$ compounds by Huyen et al., who provide a symmetry analysis of the complex magnetic structures that can arise in terms of the multipole moments of the spin distribution.[42] There are measurements in Mn_3NiN films,[61] and the anomalous Hall effect changes sign at compensation in $Mn_{4-x}Ni_xN$, when $x \approx 0.2$.[62]

An anomalous Nernst effect, the counterpart of the anomalous Hall effect for heat currents. Anomalous Nernst[63,64] and Righi-Leduc[64] effects are reported experimentally in Mn_3Sn. and a giant anomalous Nernst effect of 1.8 $AK^{-1}m^{-1}$ is calculated for Mn_3NiN.[65] A different topological spin structure in the form of skyrmions between 50 nm and 250 nm in diameter, can be introduced in Mn_4N by Dzyaloshinskii-Moriya coupling via a $Pt_{1-x}Cu_x$ overlayer.[66]

Reports of compensation in Mn_4N films have largely focused on films doped with Ni or Co on the corner sites. There is great scope for using other, nonmagnetic dopants from the third, fourth and fifth periods, which have been shown to be effective in bulk material[6] (Fig. 5). The prospects for developing thin film heterostructures, which are at the heart of ferromagnetic spintronics, is largely untapped for ferrimagnets. Magnetic tunnel junctions with a large tunnel magnetoresistance will be an important milestone, as will be an exploration of the ultra-fast spin dynamics.

Conclusions

This brief review has focussed on the magnetic aspects of metallic perovskites with interstitial nitrogen, particularly the Mn-based materials where frustrated, noncollinear magnetism is at the origin of many of their unusual physical properties. The ternary systems are so extensive and versatile that other new combinations of magnetic, electronic, thermal and mechanical effects can be expected. The systematic application of density functional theory to these systems can contribute to a rapid identification of some new opportunities, provided the frustrated non-collinear magnetic structures that arise thin films, controlled by small terms in the energy, can be calculated. It is challenging to measure them in thin films. The magnetism of manganese, which led Néel to develop the molecular field theory of antiferromagnetism 90 years ago (for which he, notoriously, could envisage no practical use) has taken a new lease of life. There is now the prospect that we could begin to enjoy the benefits of frustrated ferrimagnetic manganese in astutely-designed room temperature devices.

The 60-years timespan covered by this review provokes some reflections on how the practice of condensed matter physics has evolved in John Goodenough's lifetime. Publications with one or two authors having complete ownership and a clear message, often based on a single laboratory-based experimental method, have given way to articles with a dozen or more authors spanning two or even three generations who are specialized in just one aspect of a multifactorial experimental study. Much is published. Much is accessible provided it is written in English. Yet what was known can be forgotten or overlooked. Impact is now judged less by the novelty of the science than by the title of the journal where the work is published, frequently for the benefit of shareholders rather than stakeholders. Reliable common public knowledge and understanding of Nature remains our critical collective aim, no matter how the progress of solid state science and its applications modifies the means we have at our disposal to acquire it.

Acknowledgments

This work was supported by Science Foundation Ireland, project 16/IA/4534 ZEMS and contract 12/RC/2278_P2 AMBER. We are grateful to Yangkun He for discussions and help with the manuscript.

ORCID

J. M. D. Coey https://orcid.org/0000-0003-0053-8452

References

1. D. Fruchart, R. Fruchart, P L'Heritier, K. Kanematsu, R. Madar, S. Misawa, Y Nakamura, P. J. Webster, and K. R. A. Ziebeck, *Landolt-Bornstein, New Series, Group III: Crystal and Solid State Physics volume 19: Magnetic properties of metals, Subvolume C Alloys and compounds of d elements—Part 2 — 1.5.6 Metallic Perovskites*, ed. H. P. J. Wijn (Springer, Berlin) (1988).
2. J. M. D. Coey, *Magnetism and Magnetic Materials* Second ed.(Cambridge University Press, Cambridge) (2022).
3. A. Leineweber, T Hickel, B. Azimi-Manavi, and S. B. Maissel, *Acta Mater.*, **140**, 433 (2017).
4. B. C. Fraser, *Phys. Rev.*, **112**, 751 (1958).
5. W. J. Takei, *Phys. Rev.*, **125**, 1893 (1962).
6. R. Zhang, Y. He, D. Fruchart, J. M. D. Coey, and Z. Gerczi, *Acta Materialia* (2022).
7. D. Fruchart, D Givord, P. Convert, P l'Heritier, and J. P. Senateur, *J.Phys F: Metal Phys*, **9**, 2431 (1979).

8. D. Fruchart, P. l'Heritier, and R. Fruchart, *Mat. Res. Bull.*, **15**, 415 (1980).
9. R. Gupta, N. Pandey, A. Tayal, and M. Gupta, *AIP Adv.*, **5**, 097131 (2020).
10. M. Meinert, *J.Phys; Condens Matter*, **28**, 056006 (2015).
11. N. Terao, *J. Phys Soc Japan*, **15**, 227 (1960).
12. N. Pandey, M. Gupta, and J. Stahn, *J. Alloys Comp.*, **851**, 156299 (2021).
13. X. G. Diao, A. Y. Takeuchi, F. Garcia, R. B. Scorzelli, and H. R Rechenberg, *J. Appl. Phys.*, **85**, 4485 (1999).
14. M. Barberon, R. Madar, E. Fruchart, G. Lorthioir, and D. Fruchart, *Mat. Res. Bull.*, **5**, 903 (1970).
15. J. B. Goodenough, *Phys. Rev.*, **120**, 67 (1960).
16. J. B. Goodenough, *Conceptual Phase Diagrams and their Application to Itinerant Electron Magnetism*, Lincoln Laboratory Report MIT (1974).
17. D. Fruchart, E. F. Bertaut, F. Sayetat, M. Nasr-Eddine, R. Fruchart, and J. P. Sénateur, *Solid State Commun.*, **8**, 91 (1970).
18. D. Fruchart, E. F. Bertaut, E. Fruchart, M. Barberon, G. Lorthioir, and R. Fruchart, *Proc. Int. Conf. Magn. Moscow*, **IV**, 572 (1973).
19. D. Fruchart and E. F. Bertaut, *J. Phys Soc Japan*, **44**, 781 (1978).
20. J. P. Bouchaud, R. Fruchart, R. Pauthenet, M. Guillot, H. Bartholin, and F. Chaissé, *J. Appl. Phys.*, **37**, 971 (1966).
21. R. Madar, M. Barberon, E. Fruchart, and R. Fruchart, *C.R. Acad. Sc. Paris*, **267**, 1404 (1968).
22. R. Fruchart, R. Madar, M. Barberon, E. Fruchart, and G. Lorthioir, *J. de Physique Coll.*, **32C1**, Suppl. 2-3, 982 (1971).
23. D. Givord, Thèse de troisième cycle, *Contribution à l'étude des propriétés magnétiques des composes métalliques à structures perosvskite du manganèse* Grenoble 1969.
24. R. Burriel, L. Tocado, E. C. Palacios, T. Tohei, and H. Wada, *J. Magn. Magn. Mater.*, **290**, 715 (2005).
25. L. H. Lewis, D. Yoder, and A. R. Moodenbaugh, *J. Phys. Condens. Matter*, **18**, 1677 (2006).
26. T. Tohei, H. Wada, and T. Kanomata, *J. Appl Phys.*, **94**, 1800 (2003).
27. B. S. Wang et al., *Europhys. Lett.*, **85**, 47004 (2009).
28. D. Fruchart, Thèse d'état, Etudes par Diffraction Neutronique des Perovskites Métalliques Mn_3MX, Carbures (X = C; M = Zn, Ga, Sn), Nitrures X = N; M = Ni, Cu, Zn, Ga, Rh, Ag, Sn, Sb, Pt), Grenoble (1976).
29. E. F. Bertaut, D. Fruchart, J. P. Bouchaud, and R. Fruchart, *Solid State Comm.*, **6**, 251 (1968).
30. E. F. Bertaut, *Acta Cryst.*, **A24**, 217 (1968).
31. H. A. Zhou, T. Xu, H. Bai, and W Jiang, *J. Phys. Soc. Japan*, **90**, 081006 (2021).
32. T Suemasu, L. Vila, and J-P Attané, *J. Phys. Soc. Japan*, **90**, 081010 (2021).
33. Z. Zhang and W. Mi, *J.Phys. D; Appl. Phys*, **55**, 013001 (2022).
34. Y. Yasutomi, K. Ito, T. Sanai, K. Toku, and T. Suemasu, *J. Appl. Phys.*, **115**, 17A935 (2014).
35. T. Gushi et al., *Nano Lett.*, **19**, 8716 (2019).
36. S. Ghosh et al., *Nano Lett.*, **21**, 2580 (2021).
37. S. Isogami, N. Rajamanickam, Y. Kosuga, and Y. K. Takahashi, *AIP Adv.*, **11**, 105314 (2021).
38. T. Bayaraa, C. Xu, and L. Bellaiche, *Phys. Rev. Lett.*, **127**, 217204 (2021).
39. D. Boldrin et al., *Appl.. Mater. Interfaces*, **10**, 18863 (2018).
40. P. Lukashev and R. F. Sabtranov, *Physical Review B*, **82**, 094417 (2010).
41. J. Zemen, Z Gercsi, and K. G. Sandemann, *Phys. Rev. B*, **96**, 024491 (2017).
42. V. T. Ngoc Huyen, M. T. Suzuki, K. Yamauchi, and T. Oguchi, *Physical Review B.*, **100**, 094426 (2019).
43. H. K. Singh, I. Samathrakis, N. M. Fortunato, J. Zemen, C. Shen, O. Gutfleisch, and H. Zhang, *NPJ Comp. Mater*, **7**, 98 (2021).
44. T. Hamada and K. Takenaka, *Appl. Phys. Lett.*, **87**, 261902 (2005).
45. K. Takenaka and H. Tagaki, *Appl. Phys. Lett.*, **94**, 131904 (2009).
46. T. Shibayama and K. Takenaka, *J. Appl. Phys.*, **109**, 07A928 (2011).
47. J. Yan, Y. Sun, H. Wu, Q. Huang, C. Wang, Z. Shi, S. Deng, K. Shi, H. Lu, and L Chu, *Acta Mater.*, **74**, 58 (2014).
48. D. Matsunami, A. Fujita, K. Takenaka, and M. Kano, *Nat. Mater.*, **14**, 73 (2015).
49. D. Boldrin et al., *Phys. Rev. X*, **8**, 041035 (2018).
50. J. Zemen, E. Mendive-Tapia, Z. Gercsi, R. Banerjee, J. B. Staunton, and K. G. Sandemann, *Phys. Rev. B*, **95**, 184438 (2017).
51. H. Chen, Q. Niu, and A. H. MacDonald, *Phys. Rev. Lett.*, **112**, 017205 (2014).
52. Z. Q. Liu et al., *Nat. Electron.*, **1**, 172 (2018).
53. J. Kübler and C. Felser, *Europhys. Lett.*, **108**, 67001 (2014).
54. S. Nakatsuji, N. Kiyohara, and T. Higo, *Nature*, **527**, 212 (2015).
55. A. K. Nayak et al., *Sci. Adv.*, **2**, 1501870 (2016).
56. O. Busch, B. Gobel, and I. Mertig, *Phys. Rev. Research*, **2**, 033112 (2020).
57. Y Zhang, Y Sun., H. Yang, J. Zelezny, S. P. P. Parkin, C. Felser, and B. Yan, *Phys. Rev. B*, **95**, 075128 (2017).
58. Y. Zhang, J. Zelezny, Y. Sun, J. van den Brink, and B. Yan, *New J. Phys.*, **20**, 073028 (2018).
59. O. Busch, B. Gobel, and I. Mertig, *Phys. Rev. B*, **104**, 184423 (2021).
60. W. Zhang, W. Han, S. H. Yang, Y. Sun, Y. Zhang, B. Yan, and S. S. P. Parkin, *Sci. Adv.*, **2**, 1600759 (2016).
61. D. Boldin et al., *Phys. Rev. Mater.*, **3**, 094409 (2019).
62. T. Komori, T. Gushi, A. Anzai, L. Vila, J. P. Attané, S. Pizzini, J. Vogel, S. Isogami, K. Toko, and T. Suemasu, *J. Appl. Phys.*, **125**, 213902 (2019).
63. M. Ikhlas, T. Tomita, T. Koretsune, M. T. Suzuki., D. Nishio-Hamane, R. Arita, Y. Otani, and S. Nakatsuji, *Nat. Phys.*, **13**, 1085 (2017).
64. X. Li, L. Xu, L. Ding, J. Wang, M Shen, X. Liu, Z. Zhu, and K. Behnia, *Phys. Rev. Lett.*, **119**, 056601 (2017).
65. X. Zhou, J. P. Hanke, W. Feng, S. Blügel, Y. Mokrousov, and Y. Yao, *Phys. Rev. Mater.*, **4**, 024408 (2020).
66. C. T. Ma, T. Q. Hartnett, W. Zhou, P. V. Balachandran, and S. J. Poon, *Appl. Phys. Lett.*, **119**, 192406 (2021).
67. J. P. Jardin and J Labbé, *J. Physique*, **36**, 1317 (1975).